The Astrophysical Journal, 934:186 (12pp), 2022 August 1 https://doi.org/10.3847/1538-4357/ac7c1e

Radio Evolution of a Type IIb Supernova SN 2016gkg

Nayana A. J.[1], Poonam Chandra[2,3], Anoop Krishna[4], and G. C. Anupama[1]
[1] Indian Institute of Astrophysics, II Block, Koramangala, Bangalore 560034, India; nayana.aj@iiap.res.in
[2] National Radio Astronomy Observatory, 520 Edgemont Road, Charlottesville, VA 22903, USA
[3] National Centre for Radio Astrophysics, Tata Institute of Fundamental Research, PO Box 3, Pune, 411007, India
[4] N.S.S College, Ottapalam, Palakkad 679103, India
Received 2022 April 6; revised 2022 June 15; accepted 2022 June 23; published 2022 August 5

Abstract

We present extensive radio monitoring of a Type IIb supernova (SN IIb), SN 2016gkg during $t \sim 8-1429$ days postexplosion at frequencies $\nu \sim 0.33-25$ GHz. The detailed radio light curves and spectra are broadly consistent with self-absorbed synchrotron emission due to the interaction of the SN shock with the circumstellar medium. The model underpredicts the flux densities at $t \sim 299$ days postexplosion by a factor of 2, possibly indicating a density enhancement in the circumstellar medium due to a nonuniform mass loss from the progenitor. Assuming a wind velocity $v_w \sim 200\,\mathrm{km\,s^{-1}}$, we estimate the mass-loss rate to be $\dot{M} \sim$ (2.2, 3.6, 3.8, 12.6, 3.7, and 5.0) $\times$ $10^{-6}\ M_\odot\,\mathrm{yr^{-1}}$ during ~8, 15, 25, 48, 87, and 115 yr, respectively, before the explosion. The shock wave from SN 2016gkg is expanding from $R \sim 0.5 \times 10^{16}$ to 7×10^{16} cm during $t \sim 24-492$ days postexplosion indicating a shock deceleration index, $m \sim 0.8$ ($R \propto t^m$), and mean shock velocity $v \sim 0.1c$. The radio data are inconsistent with a free–free absorption model and higher shock velocities are in support of a relatively compact progenitor for SN 2016gkg.

Unified Astronomy Thesaurus concepts: Supernovae (1668); Circumstellar matter (241); Radio continuum emission (1340)

1. Introduction

Type IIb supernovae (SNe IIb) are a subclass of core-collapse supernovae (CCSNe) characterized by the presence of broad H I absorption features in the early optical spectra. At later times, these H I lines disappear and the He I feature becomes dominant in the spectra (Filippenko 1997), placing SNe IIb in between hydrogen-rich Type II SNe and hydrogen poor Type Ibc SNe. The progenitors of SNe IIb are understood to be stars that have lost most of their hydrogen envelope but not all. The hydrogen envelope could be lost either via radiatively driven winds (Smith & Conti 2008) or via mass transfer by a binary companion (Yoon et al. 2010).

Progenitor candidates have been identified for a few SNe IIb from preexplosion images: a K-type supergiant in a binary system for SN 1993J (Aldering et al. 1994; Maund et al. 2004), a yellow supergiant for SN 2011dh (Arcavi et al. 2011; Maund et al. 2011; Sahu et al. 2013; Van Dyk et al. 2013), and a massive star of mass $M \sim 20-25\ M_\odot$ for SN 2008ax (Crockett et al. 2008; Taubenberger et al. 2011). Besides these direct detection efforts, the luminosity evolution of an early light curve that maps the cooling envelope phase after the shock breakout can also put constraints on mass and radius of the progenitor star (Baron et al. 1993; Swartz et al. 1993).

Independent constraints on the progenitor properties can be obtained by studying the nonthermal radio emission from SNe IIb that arises as a result of the dynamical interaction between the supernova (SN) shock and the circumstellar medium (CSM; Chevalier 1982, 1998). Radio observations uniquely probe the density structure of the CSM and thereby a longer period of mass loss of the progenitor star (Weiler et al. 1986; Chevalier 1982, 1998). Several SNe IIb exhibit luminous radio emission; a few examples are SN 1993J (Weiler et al. 2007), SN 2001gd (Stockdale et al. 2003, 2007), SN 2001ig (Ryder et al. 2004), SN 2003bg (Soderberg et al. 2006), SN 2011dh (Krauss et al. 2012; Soderberg et al. 2012), SN 2011hs (Bufano et al. 2014), and SN 2013df (Kamble et al. 2016).

Chevalier & Soderberg (2010) compiled a sample of radio bright SNe IIb and divided them based on their radio properties. The authors proposed two populations of SNe IIb; one with compact progenitors (SNe cIIb) and the other with extended progenitors (SNe eIIb). The SNe cIIb group shows faster shock velocities, less dense CSM, and compact progenitors in comparison with that of SNe eIIb. However, there exist a few examples (e.g., SN 2011dh; Bersten et al. 2012; Horesh et al. 2013; Maeda et al. 2014) that suggest that the radio properties may or may not be a good indicator of the progenitor size. The progenitors of SNe IIb could be a continuum of objects between compact and extended stars instead of a sharp split like SNe eIIb and SNe cIIb.

This paper presents the radio follow-up observations of a Type IIb supernova (SN IIb) SN 2016gkg from $t \sim 8$ to 1429 days over a frequency range of 0.3–25 GHz. The data include our observations taken with the Giant Metrewave Radio Telescope (GMRT) and the archival data from the Jansky Very Large Array (JVLA). We model the radio emission to investigate the mass-loss history of the progenitor system, the evolution of SN shock radius and magnetic field, and irregularities in the CSM density.

The paper is organized as follows. In Section 2, we present the compilation of various results on SN 2016gkg from the literature. The details of observations and data reduction are presented in Section 3. We discuss the radio emission model and derive various parameters of the progenitor and environments in Section 4 and Section 5. The results are discussed in Section 6 and conclusions are drawn in Section 7.

2. SN 2016gkg

SN 2016gkg was discovered by Buso & Otero on 2016 September 20.18 (UT)[5] at a position $\alpha_{J2000} = 01^h34^m14^s.40$, $\delta_{J2000} = -29°26'24''.20$. The SN is located at a distance of 26.4 ± 5.3 Mpc in the galaxy NGC 613 (Nasonova et al. 2011). The SN was classified as a SN IIb based on the optical spectroscopic observations (Tartaglia et al. 2017). Kilpatrick et al. (2017) model the early time optical light curve of SN 2016gkg and derive the date of explosion to be $t_0 = 2016$ September $20.15^{+0.08}_{-0.10}$ UT. We adopt this as the date of explosion throughout this paper and all epochs t mentioned are with respect to t_0.

SN 2016gkg was extensively followed in the optical bands soon after the discovery that provided excellent coverage of its early evolution. The SN showed a double peak structure in the optical light curve, the early peak due to the shock cooling of the hydrogen envelope of the progenitor star, and the later peak powered by radioactive decay (Kilpatrick et al. 2017; Tartaglia et al. 2017; Bersten et al. 2018). Preexplosion images of the field containing SN 2016gkg taken in 2001 with the Hubble Space Telescope (HST) Wide Field Planetary-Camera 2 (WFPC2) is available in the archive (Bersten et al. 2018).

Various groups (Arcavi et al. 2017; Kilpatrick et al. 2017; Piro et al. 2017; Tartaglia et al. 2017; Bersten et al. 2018) attempted to constrain the properties of the progenitor of SN 2016gkg by modeling the early peak of the light curve by shock cooling models. The progenitor radius estimates from these studies span a wide range $R_* \sim 40$–646 $R_\odot$ depending on the model and assumed structure of the hydrogen envelope of the progenitor. Piro et al. (2017) investigated the early peak of the optical light curve by numerically exploding a large number of extended envelope models and constraining the radius to be $R_* \sim$ 180–260 $R_\odot$. Arcavi et al. (2017) fit the observed light curve with analytical shock cooling models (Nakar & Piro 2014; Piro 2015; Sapir & Waxman 2017) and estimated the progenitor radius to be $R_* \sim 40$–150 $R_\odot$. Bersten et al. (2018) modeled the cooling peak and estimated the radius of the hydrogen envelope to be $\sim$320 $R_\odot$. Modeling the initial rapid rise of the light curve using the Rabinak & Waxman (2011) model, Kilpatrick et al. (2017) constrained the progenitor radius to be $R_* = 257^{+389}_{-189}$. Tartaglia et al. (2017) modeled the temperature evolution of initial peak of the light curve and estimated the progenitor radius to be $R_* \sim 48-124$ $R_\odot$.

Kilpatrick et al. (2017) detected a progenitor candidate of SN 2016gkg in the archival HST image and estimated the luminosity and radius to be $\log(L/L_\odot) = 5.15$ and $R_* = 138^{+131}_{-103}$ $R_\odot$, respectively. The authors found that single star stellar evolution models fail to reproduce the derived progenitor properties whereas binary evolutionary tracks could reproduce them. Tartaglia et al. (2017) identified two plausible progenitor candidates from HST imaging analysis and suggested a range of progenitor mass $15-20$ $M_\odot$ and radius $(150-320)$ $R_\odot$. Kilpatrick et al. (2021) present postexplosion late-time ($t \sim 652-1795$ days) HST observations of SN 2016gkg and their improved astrometric alignment between the SN and progenitor candidate allowed them to constrain the progenitor to be a compact yellow supergiant of radius $\sim$70 $R_\odot$ with effective temperature ($T_{\rm eff}$) $\sim$10,800 K. Late-time ($t \sim 300$–800 days) spectroscopic observations of SN 2016gkg reveal multicomponent emission lines indicating the presence of material with different velocities possibly indicating an asymmetric explosion (Kuncarayakti et al. 2020).

Table 1
Details of GMRT Observations of SN 2016gkg

Date of Observation (UT)	Age[a] (Day)	Frequency (GHz)	Flux density (mJy)[b]
2016 Nov 09.76	50.61	1.39	0.36 ± 0.08
2016 Dec 10.64	81.49	1.39	0.44 ± 0.07
2017 Apr 30.16	222.01	1.39	1.65 ± 0.18
2017 Sep 08.83	353.68	1.39	1.38 ± 0.15
2017 Nov 23.63	429.48	1.39	1.13 ± 0.12
2018 Jun 12.98	630.83	1.39	0.78 ± 0.10
2018 Sep 08.85	718.70	1.39	0.75 ± 0.09
2019 Jan 27.45	859.30	1.39	0.69 ± 0.09
2020 Aug 07.09	1416.94	1.39	0.59 ± 0.10
2016 Dec 12.57	83.42	0.61	<0.18
2017 Apr 29.29	221.14	0.61	0.44 ± 0.09
2017 Sep 08.83	353.68	0.61	1.11 ± 0.15
2017 Nov 23.63	429.48	0.61	1.67 ± 0.20
2018 Jun 10.85	628.70	0.61	1.51 ± 0.34
2018 Sep 09.83	719.68	0.61	1.60 ± 0.21
2019 Jan 28.41	860.26	0.61	1.43 ± 0.44
2019 Aug 20.92	1064.77	0.61	1.32 ± 0.23
2020 Aug 05.05	1414.90	0.61	1.18 ± 0.32
2020 Aug 18.82	1428.67	0.325	$\leqslant 3$

Notes.
[a] The age is calculated assuming 2016 September 20.15 (UT) as the date of explosion (Kilpatrick et al. 2017).
[b] The errors on the flux densities are the sum of error from task JMFIT and a 10% calibration uncertainty added in quadrature.

3. Observations and Data Reduction

3.1. GMRT Observations

We carried out regular monitoring of SN 2016gkg with the GMRT during $t \sim 51$–1429 days at 0.33, 0.61, and 1.39 GHz. The data were recorded with an integration time of 16 s in full polar mode with a bandwidth of 33 MHz, split into 256 channels; 3C 286 and 3C 147 were used as the flux density calibrators and J0240−2309 was used as the phase calibrator.

The GMRT data were inspected and calibrated using the astronomical image processing software (Greisen 2003) following standard procedure (see Nayana et al. 2017). The calibrated visibilities were imaged excluding the short uv data to minimize the contribution from the extended host galaxy emission. The host galaxy is of flux density $\sim$178.3 mJy at 1.4 GHz with an angular size $\sim 48.5 \times 30.4$ arcsec^2 in the NVSS map (Condon et al. 1998). The flux density of the SN was determined by fitting a Gaussian at the source position using task JMFIT.[6] The SN is $\sim$92 arcsec away from the center of the host galaxy, well beyond the continuum emission from the galaxy. However, we fit a zero-level baseline while fitting the Gaussian to account for any residual emission from the host galaxy. The details of GMRT observations are given in Table 1. The errors on flux densities quoted in Table 1 are the sum of map rms values and a 10% calibration uncertainty added in quadrature. The upper limits on radio flux densities

[5] http://ooruri.kusastro.kyoto-u.ac.jp/mailarchive/vsnet-alert/20188

[6] http://www.aips.nrao.edu/cgi-bin/ZXHLP2.PL?JMFIT

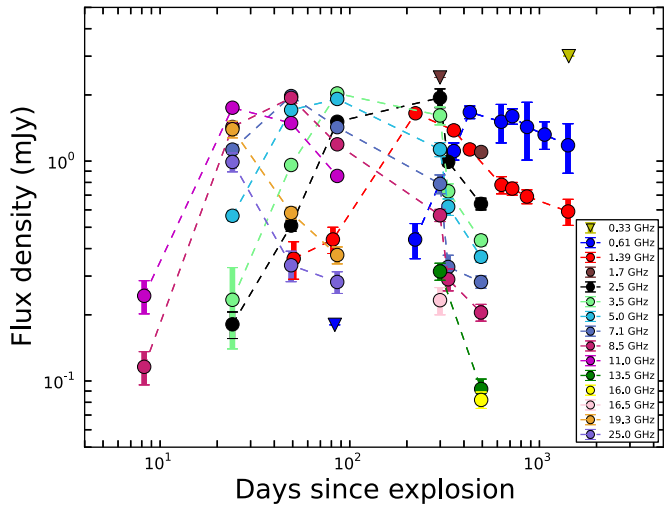

Figure 1. The GMRT and JVLA light curves of SN 2016gkg at frequencies 0.33–25 GHz. The inverted triangle denotes 3σ upper limits. The age of the SN is calculated assuming the date of explosion to be 2016 September 20.15 UT (Kilpatrick et al. 2017).

are three times the map rms at the supernova position. The GMRT light curves are shown in Figure 1.

3.2. JVLA Observations

The Karl G. JVLA observed SN 2016gkg during $t \sim 8$–492 days covering a frequency range 2–25 GHz (archival data; PI: Maria Drout). The observations were done in standard continuum mode with a bandwidth of 2.048 GHz split into 16 spectral windows each of 128 MHz; 3C 147 was used as the flux density calibrator, and J0145−2733 was used as the phase calibrator.

The JVLA archival data were reduced using standard packages in common astronomy software applications (CASA; McMullin et al. 2007). We use the CASA task TCLEAN for imaging and we exclude short baselines to minimize the host galaxy emission while imaging. The flux density of the source is estimated by fitting a Gaussian at the source position using task IMFIT. The details of JVLA observations are given in Table 2. The errors on flux densities quoted in Table 1 are the sum of map rms values and 10% calibration uncertainties added in quadrature. Figure 1 shows the flux density evolution of SN 2016gkg at frequencies 2−25 GHz.

4. Radio Emission Model

The general properties of radio emission from CCSNe have been discussed in detail by Chevalier (1982, 1998) and Weiler et al. (1986, 2002). The radio light curves and spectra can be described using the "mini-shell" model (Chevalier 1982, standard model). According to this model, the forward shock from the SN interacts with the ionized CSM established due to the stellar winds of the progenitor star. At the shock, particles are accelerated to relativistic velocities in amplified magnetic fields and emit synchrotron radiation. A fraction of postshock energy density is distributed into magnetic fields (ϵ_B) and relativistic electrons (ϵ_e), and this fraction is assumed to be constant throughout the evolution of the ejecta. The observed radio light curves/spectra will be characterized by synchrotron radiation, where the low-frequency emission is significantly suppressed by an absorption component. The absorption can be

Table 2
Details of JVLA Observations of SN 2016gkg

Date of Observation (UT)	Age[a] (Day)	Frequency (GHz)	VLA Array	Flux density (mJy)[b]
2016 Sep 28.39	8.24	8.549	A	0.116 ± 0.023
	8.24	10.999	A	0.244 ± 0.049
2016 Oct 14.21	24.06	2.499	A	0.181 ± 0.031
	24.06	3.499	A	0.234 ± 0.097
	24.06	4.999	A	0.564 ± 0.063
	24.06	7.099	A	1.128 ± 0.115
	24.06	8.549	A	1.430 ± 0.151
	24.06	10.999	A	1.749 ± 0.184
	24.06	19.299	A	1.396 ± 0.184
	24.06	24.999	A	0.991 ± 0.139
2016 Nov 08.21	49.06	2.499	A	0.509 ± 0.059
	49.06	3.499	A	0.960 ± 0.104
	49.06	4.999	A	1.708 ± 0.174
	49.06	7.099	A	1.976 ± 0.201
	49.06	8.549	A	1.939 ± 0.197
	49.06	10.999	A	1.489 ± 0.154
	49.06	19.299	A	0.581 ± 0.068
	49.06	24.999	A	0.336 ± 0.063
2016 Dec 15.01	85.86	2.499	A	1.510 ± 0.033
	85.86	3.499	A	2.031 ± 0.208
	85.86	4.999	A	1.917 ± 0.193
	85.86	7.099	A	1.427 ± 0.144
	85.86	8.549	A	1.192 ± 0.123
	85.86	10.999	A	0.856 ± 0.089
	85.86	19.299	A	0.374 ± 0.050
	85.86	24.999	A	0.282 ± 0.043
2017 Mar 19.84	299.08	1.749	D	<2.4
	299.08	2.499	D	1.940 ± 0.272
	299.08	3.499	D	1.612 ± 0.220
	299.08	4.999	D	1.131 ± 0.140
	299.08	7.099	D	0.788 ± 0.110
	299.08	8.549	D	0.567 ± 0.067
	299.08	9.499	D	0.485 ± 0.064
	299.08	13.499	D	0.315 ± 0.042
	299.08	16.499	D	0.233 ± 0.040
2017 Aug 16.44	330.29	2.499	C	0.992 ± 0.108
	330.29	3.499	C	0.729 ± 0.094
	330.29	4.999	C	0.620 ± 0.082
	330.29	7.099	C	0.330 ± 0.054
	330.29	8.549	C	0.290 ± 0.044
	330.29	9.499	C	0.270 ± 0.035
2018 Jan 25.04	491.89	2.499	B	0.639 ± 0.075
	491.89	3.499	B	0.436 ± 0.050
	491.89	4.999	B	0.367 ± 0.042
	491.89	7.099	B	0.282 ± 0.033
	491.89	8.549	B	0.205 ± 0.027
	491.89	9.499	B	0.200 ± 0.024
2018 Jan 26.04	492.89	1.749	B	1.100 ± 0.112
	492.89	13.499	B	0.092 ± 0.014
	492.89	15.999	B	0.082 ± 0.011

Notes.
[a] The age is calculated using 2016 September 20.15 (UT) as the date of explosion (Kilpatrick et al. 2017).
[b] The errors on the flux densities are the sum of error from task IMFIT and a 10% calibration uncertainty added in quadrature.

free–free absorption (FFA) due to the ionized wind material along the line of sight (Weiler et al. 1986) or due to the same relativistic electrons that generate radio emission (synchrotron self-absorption; SSA; Chevalier 1998). The radio flux density initially rises rapidly and then declines as a result of the

combined effects of nonthermal synchrotron emission and various absorption processes.

This standard model of hydrodynamic evolution of ejecta assumes self-similar evolution of physical parameters across the shock (Chevalier 1996). The shock radius evolves as $R \sim t^m$ where $m = (n-3)/(n-s)$, and n indicates the outer density profile of the SN ejecta ($\rho_{\rm ejecta} \propto r^{-n}$); s denotes the density profile of the CSM ($\rho_{\rm CSM} \propto r^{-s}$) and the value of $s = 2$ for a wind stratified medium.

We adopt the model from Weiler et al. (1986) in a scenario where the dominant absorption process is FFA and follow a similar method as discussed in Nayana et al. (2018) and Nayana & Chandra (2020). In an FFA model, the spectral and temporal evolution of radio flux densities $F(\nu, t)$ can be described as:

$$F(\nu, t) = K_1 \left(\frac{\nu}{5\ \rm GHz}\right)^{\alpha} \left(\frac{t}{10\ \rm days}\right)^{\beta} e^{-\tau_{\rm FFA}}, \quad (1)$$

$$\tau_{\rm FFA} = K_2 \left(\frac{\nu}{5\ \rm GHz}\right)^{-2.1} \left(\frac{t}{10\ \rm days}\right)^{\delta}. \quad (2)$$

The multifrequency radio flux density evolution in the case of a dominant SSA scenario can be modeled as (Chevalier 1998)

$$F(\nu, t) = K_1 \left(\frac{\nu}{5\ \rm GHz}\right)^{2.5} \left(\frac{t}{10\ \rm days}\right)^{a} [1 - e^{-\tau_{\rm SSA}}], \quad (3)$$

$$\tau_{\rm SSA} = K_2 \left(\frac{\nu}{5\ \rm GHz}\right)^{-(p+4)/2} \left(\frac{t}{10\ \rm days}\right)^{-(a+b)}. \quad (4)$$

In the above equations, K_1 and K_2 denote the flux density and optical depth at 5 GHz on $t = 10$ days postexplosion, respectively. In Equations (1) and (2), α represents the spectral index ($F_\nu \propto \nu^{\alpha}$) and β represents the temporal index of radio flux densities. The term $\exp(-\tau_{\rm FFA})$ corresponds to the attenuation due to the absorption by a uniformly distributed ionized CSM external to the radio emitting region; "δ" denotes the temporal evolution of $\tau_{\rm FFA}$, and is related to α and β as $\delta = \alpha - \beta - 3$. Assuming the CSM is created due to a steady stellar wind ($\rho_{\rm CSM} \propto r^{-2}$), the shock deceleration parameter m can be written as $m = -\delta/3$ where $m = (n-3)/(n-2)$.

In Equations (3) and (4), a and b denote the temporal indices of flux densities in the optically thick ($F \propto t^{a}$) and thin phase ($F \propto t^{-b}$), respectively; $\tau_{\rm SSA}$ is the optical depth due to SSA and p is the electron energy power-law index ($N(E) \propto E^{-p}$), which is related to α as $p = 2\alpha - 1$. In an SSA model "m" is connected to a, b, and p as $a = 2m + 0.5$ in the optically thick phase and $b = (p + 5 - 6m)/2$ in the optically thin phase (Chevalier 1998).

We perform a two variable fit to the entire data to find the best parameter fit to the FFA model using Equations (1) and (2) and the SSA model using Equations (3) and (4). We execute the fit adopting the Markov Chain Monte Carlo (MCMC) method using python package *emcee* (Foreman-Mackey et al. 2013). We choose 32 walkers and 5000 steps to explore the parameter space to get the best-fit values (68% confidence interval). We estimate the goodness of fit using the reduced χ^2_μ test. We allow the parameters K_1, K_2, α, β, and δ to vary freely in the FFA model, and K_1, K_2, a, b, and p to vary freely in the SSA model. The best-fit values of these parameters are listed in Table 3. The best-fit modeled curves along with the observed data points are shown in Figures 2 and 3. The corner plots are presented in Figure 4.

Table 3
Best-fit Parameters for FFA and SSA Models

FFA	SSA
$K_1 = 13.44^{1.12}_{-0.99}$	$K_1 = 0.06^{0.00}_{-0.00}$
$K_2 = 11.97^{0.63}_{-0.58}$	$K_2 = 207.04^{25.00}_{-20.80}$
$\alpha = -1.04^{0.03}_{-0.03}$	$a = 2.33^{0.04}_{-0.04}$
$\beta = -0.93^{0.02}_{-0.02}$	$b = 0.94^{0.02}_{-0.02}$
$\delta = -1.88^{0.02}_{-0.03}$	$p = 3.03^{0.05}_{-0.05}$
$\chi^2 = 4.4$	$\chi^2 = 3.2$

From the best-fit modeled curves and reduced χ^2_μ values, the SSA model ($\chi^2_\mu = 3.2$) seems like a better representation of the observed data compared to the FFA model ($\chi^2_\mu = 4.4$). However, there are deviations from SSA model predictions, particularly at $t \sim 299$ days. The model underestimates the flux densities at multiple frequencies (see Figure 2). This effect is clear in the spectrum of day 299 where all the flux densities in the optically thin regime are systematically above the modeled curve (see Figure 3). We discuss this effect in the context of a CSM density enhancement in Section 5.

The best-fit value of the shock deceleration parameter is $m \sim 0.6$ ($m = -\delta/3$) in the FFA model. This is fairly low compared to the typical m values seen in SNe IIb and would imply a highly decelerating shock wave, which is unphysical at this early stage of evolution. The value of $m \sim 1$ from the SSA model [$m = (p + 5 - 2b)/6$], which is indicative of a non-decelerating blast wave. Thus we infer the SSA model to be a better representation of the data over the FFA model due to lower χ^2_μ values and the unrealistic m value implied by the FFA model.

The low-frequency flux measurements at earlier epochs (t $\sim$ 24 and 49 days) are above the model predictions (see Figure 3). The spectral indices of the flux densities between 0.61 and 1.39 GHz are 0.76 ± 0.45 and 0.59 ± 0.25 at $t \sim 24$ and 49 days, respectively. These values are flatter than the expected spectral indices ($\alpha = 2.5$) in a standard SSA model. This can be attributed to the inhomogeneities in the magnetic fields and/or relativistic electron distribution in the emitting region (Björnsson & Keshavarzi 2017; Chandra et al. 2019; Ho et al. 2019; Nayana & Chandra 2021).

4.1. Single Epoch Spectral Analysis

To further investigate the time evolution of shock parameters, we model each of the single epoch spectra adopting the SSA model. The functional form of the SSA spectrum can be parametrized as (Soderberg et al. 2006)

$$F_\nu = 1.582\ F_p \left(\frac{\nu}{\nu_p}\right)^{5/2} \left(1 - \exp\left[-\left(\frac{\nu}{\nu_p}\right)^{-(5-2\alpha)/2}\right]\right). \quad (5)$$

We model single epoch spectra by allowing peak frequency (ν_p), peak flux density (F_p), and α to vary freely and independently. The spectra are well fitted by an SSA model with χ^2_μ values of 0.7–3.3 (see Figure 5 and Table 4). We attempted modeling the data with the FFA model as well and the fits resulted in higher χ^2_ν values.

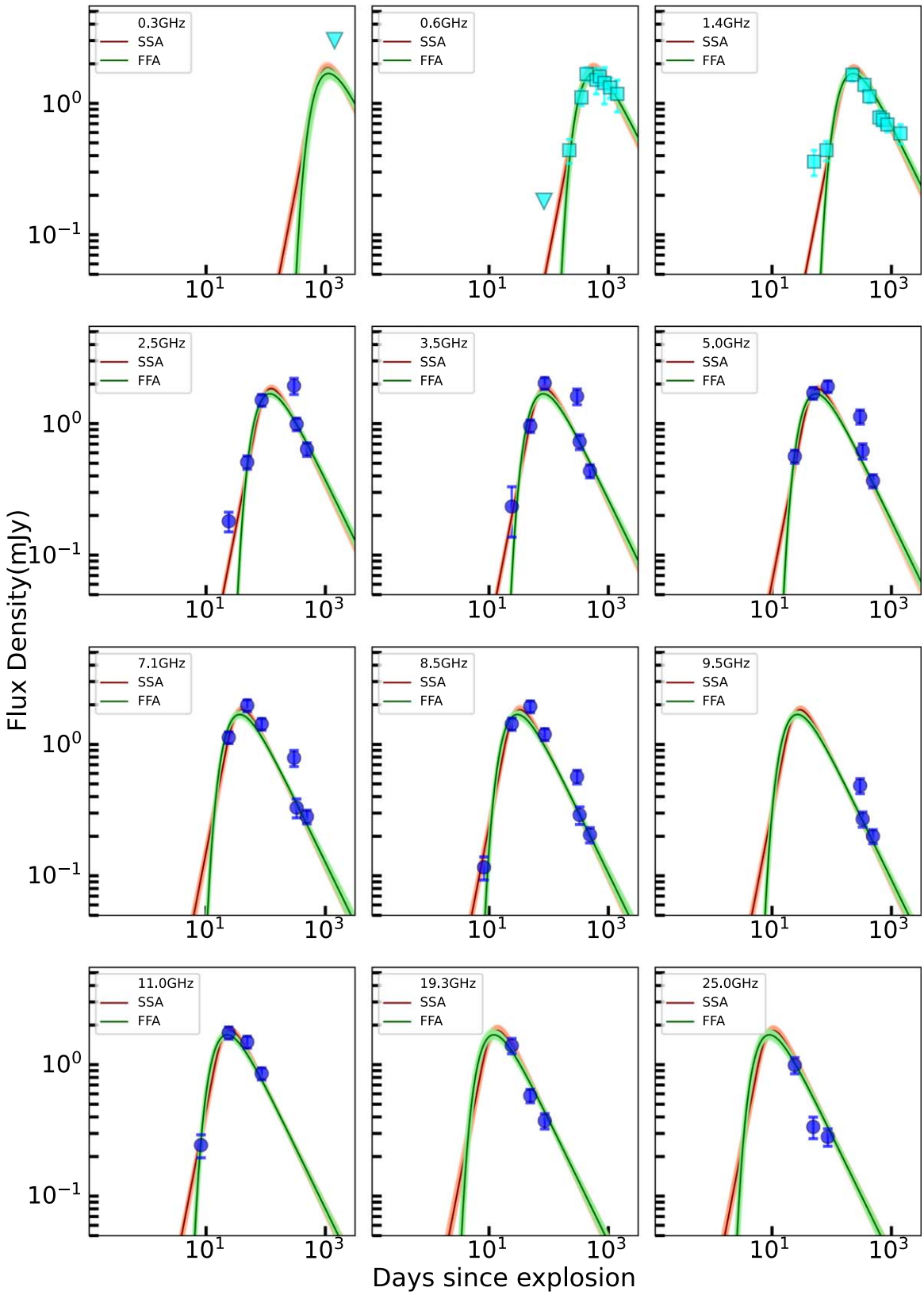

Figure 2. Radio light curves of SN 2016gkg at frequencies $\nu = 0.33$–24 GHz. The solid red curves represent the best-fit synchrotron self-absorption (SSA; Equations (3) and (4)) model and solid green curves represent the best-fit free–free absorption (FFA; Equations (1) and (2)) model (see Section 4). The light green (FFA) and red (SSA) lines represent 100 random draws from the MCMC posterior. The filled blue circles denote the JVLA flux density measurements and the filled cyan squares are GMRT flux density measurements. The inverted triangles denote 3σ flux density upper limits. The fit is a 2D fit performed by including the entire data set. The age of the SN is calculated assuming the date of explosion to be 2016 September 20.15 UT (Kilpatrick et al. 2017).

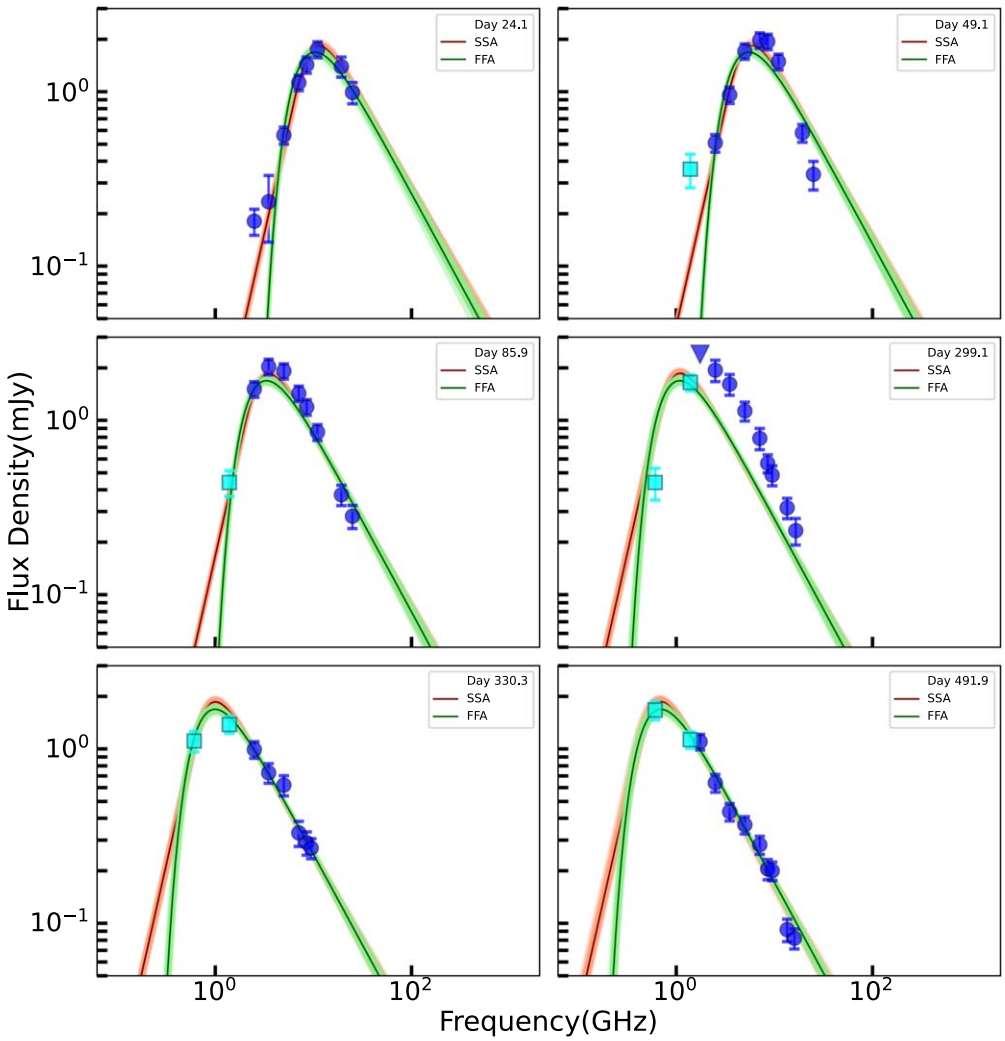

Figure 3. Radio spectra of SN 2016gkg at $t \sim 24$, 49, 86, 299, 330, and 492 days postexplosion. The solid red curves represent the best-fit synchrotron self-absorption (SSA; Equations (3) and (4)) model and solid green curves represent the best-fit free–free absorption (FFA; Equations (1) and (2)) model (see Section 4). The light green (FFA) and red (SSA) lines represent 100 random draws from the MCMC posterior. The filled blue circles denote the JVLA flux density measurements and the filled cyan squares are GMRT flux density measurements. The fit is a 2D fit performed by including the entire data set. The age of the SN is calculated assuming the date of explosion to be 2016 September 20.15 UT (Kilpatrick et al. 2017).

The best-fit F_p, ν_p, and α for the SSA model are given in Table 4. The quoted errors are 1σ errors (68% confidence interval). The temporal evolution of $\nu_{\rm p}$ and $F_{\rm p}$ are such that $\nu_{\rm p} \propto t^{-0.9}$ and $F_{\rm p} \propto t^{-0.02}$, respectively, consistent with the SSA model (Chevalier 1998). We obtain the average spectral index over six epochs as $\alpha \approx -1$. The power-law index of electrons determined from the optically thin spectral index (α) is $p = 3$ ($\alpha = -(p-1)/2$).

4.2. Blast-wave Parameters

The shock radius (R) and magnetic fields (B) can be estimated from $\nu_{\rm p}$ and $F_{\rm p}$ at each epoch (Chevalier 1998). For $p = 3$, the shock radius is given by

$$R = 8.8 \times 10^{15} f_{\rm eB}^{-1/19} \left(\frac{f}{0.5}\right)^{-1/19} \left(\frac{F_p}{\rm Jy}\right)^{9/19} \times \left(\frac{D}{\rm Mpc}\right)^{18/19} \left(\frac{\nu_p}{5\ \rm GHz}\right)^{-1} \rm cm. \quad (6)$$

The postshock magnetic field is given by

$$B = 0.58 f_{\rm eB}^{-4/19} \left(\frac{f}{0.5}\right)^{-4/19} \left(\frac{F_p}{\rm Jy}\right)^{-2/19} \times \left(\frac{D}{\rm Mpc}\right)^{-4/19} \left(\frac{\nu_p}{5\ \rm GHz}\right) \rm G. \quad (7)$$

Here, $f_{\rm eB}$ denotes the ratio of the fraction of shock energy in relativistic electrons (ϵ_e) to that in the magnetic fields (ϵ_B). We assume the equipartition of energy between relativistic electrons and magnetic fields and hence use $f_{\rm eB} = 1$; f is the volume filling factor of the synchrotron emitting region, taken to be 0.5 (Chevalier 1998). D is the distance to the SN in megaparsec. The mean velocity of the shock at any epoch is $V \sim \frac{R}{t}$.

The mass-loss rates can be deduced using the magnetic field scaling relation (Chevalier 1998);

$$\dot{M} = \frac{B^2 R^2 v_w}{2 \epsilon_B V^2}. \quad (8)$$

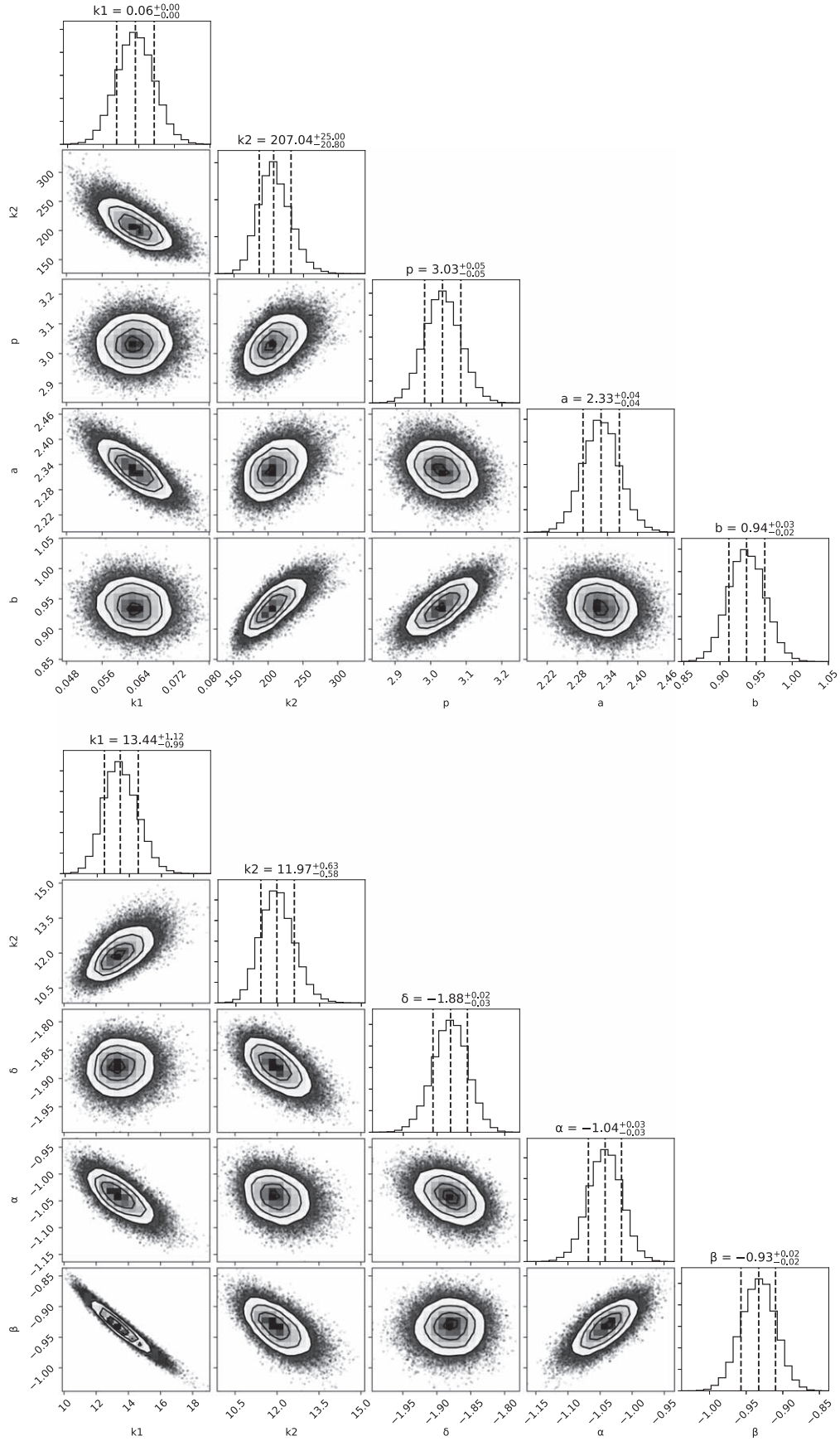

Figure 4. Corner plots that show the results of MCMC modeling of the radio data with the SSA model (Equations (3) and (4)) in top panel and FFA model (Equations (1) and (2)) in bottom panel as discussed in Section 4. The 16, 50, and 84 percentiles are marked in each of the contours and histograms.

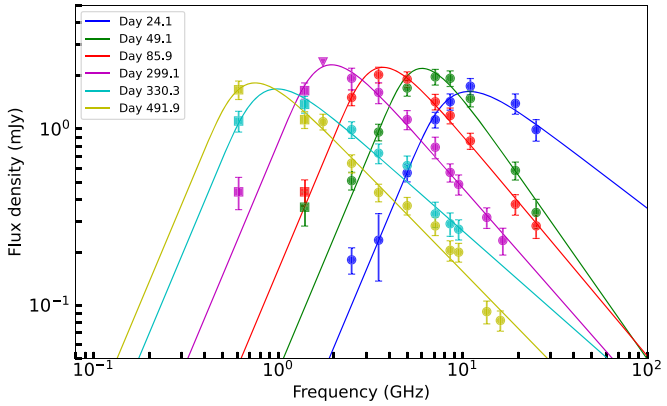

Figure 5. Radio spectra of SN 2016gkg at $t \sim 24$, 49, 86, 299, 330, and 492 days postexplosion. The filled circles denote the JVLA flux density measurements and the filled squares are near-simultaneous flux density measurements from the GMRT. The solid curves are the best-fit SSA models at each epoch.

We deduce the shock radius (R) and magnetic fields (B) at multiple epochs using the best-fit $\nu_{\rm p}$ and $F_{\rm p}$ values at $t \sim 24$, 49, 86, 299, 330, and 492 days using Equations (6) and (7). The physical parameters are presented in Table 4. The shock wave expands from $R \sim 0.5 \times 10^{16}$ cm to $R \sim 7.3 \times 10^{16}$ cm during $t \sim 24$ to 492 days. The temporal evolution of shock radius can be described by an index $m = 0.80 \pm 0.08$, indicating a decelerating blast wave (see Figure 6). The shock is slightly slowing down at $t \sim 299$ days and later evolves consistent with the temporal evolution as described by the previous phases ($t < 299$ days). The temporal index for the postshock magnetic field is found to be $\alpha_{\rm B} = -0.80 \pm 0.09$ ($B \propto t^{\alpha_{\rm B}}$).

The mass-loss rate of the progenitor star at different epochs is estimated using Equation (8). We assume a wind velocity $v_{\rm w} \sim 200\,{\rm km\,s^{-1}}$ and $\epsilon_{\rm B} = 0.33$ in the calculation. The mass-loss rates are $\dot{M} \sim (2.2\text{–}5.0) \times 10^{-6}\,M_{\odot}\,{\rm yr^{-1}}$ during 15–115 yr before explosion (see Table 4). Besides, we note that the mass-loss rate derived from the shock parameters at $t \sim 299$ days is relatively high, $\dot{M} \sim 12.6 \times 10^{-6}\,M_{\odot}\,{\rm yr^{-1}}$, indicating a higher mass loss at ~48 yr prior to explosion. Considering the uncertainty due to the low temporal cadence of the radio observations, the timing of the enhanced mass-loss event could be between 25−87 yr prior to explosion. Hydrodynamic wave driven outbursts during the late nuclear burning stage can create density enhancements in the CSM. However, these outbursts happen at 1–2 yr prior to explosion in the case of SNe IIb (Fuller & Ro 2018), which does not match with the timescales of enhanced mass loss in SN 2016gkg.

The $\dot{M}$ estimates will considerably vary depending on the choice of wind velocity. We choose $v_{\rm w} \sim 200\,{\rm km\,s^{-1}}$ based on the physical properties of the progenitor star ($M \sim 10\ M_{\odot}$, $R_{*} \sim 70\ R_{\odot}$, $T_{\rm eff} \sim 10800$ K) derived from preexplosion imaging analysis (Kilpatrick et al. 2021). The escape velocity of a 10 $M_{\odot}$ star of radius 70 $R_{\odot}$ is ~200 km s^{-1} and the range of wind velocity of a star of $T_{\rm eff} \sim 10{,}800$ K is $v_{\rm w}$ ~100−300 km s^{-1} (Drout et al. 2009; Smith 2014; Yoon et al. 2017).

5. Nonuniform Density of the CSM

The overall evolution of radio light curves and spectra of SN 2016gkg is best modeled by a self-absorbed synchrotron emission that arises due to the interaction of SN shock with the CSM created by a uniform mass loss from the progenitor. However, there are some deviations from the smooth light-curve/spectra evolution as prescribed by the standard model. There is a fractional increase by a factor of ~2 in flux densities (in the optically thin phase) at different frequencies on day 299 above the model prediction (see Figures 2 and 3). This abrupt rise in flux densities could be due to the interaction of the forward shock with density enhancements in the CSM at a radius $R \sim 3.1 \times 10^{16}$ cm. These density fluctuations could be either due to the nonuniform mass-loss rate of a single star progenitor via stellar winds and/or due to the mass stripping by a binary companion (Soderberg et al. 2006). There are several observational pieces of evidence from supernova remnants and massive stars that support complex mass-loss events happening toward the end stages of stellar evolution (Soderberg et al. 2006). In the case of a binary scenario, the strength and position of CSM density enhancement will be influenced by the binary parameters (Podsiadlowski et al. 1992). A buildup of CSM material can happen at particular spatial scales due to the modulation of progenitor stellar wind depending on the orbital period of the binary companion (Weiler et al. 1992) and the eccentricity of the binary orbit. A binary scenario with a period of 4000 yr has been attributed to the periodic modulations in the radio light curves of SN 1979C (Weiler et al. 1992; Montes et al. 2000).

Multiple episodes of mass-loss events have been attributed to periodic light-curve bumps of modest (factor of ~2) flux density fluctuations in SN 2003bg (Soderberg et al. 2006) and SN 2001ig (Ryder et al. 2004). Both these SNe showed variations in the light curve during a period $t = 120\text{−}300$ days (see Figure 8), indicating a radial distance of 4×10^{16} to 8×10^{16} cm from the explosion center, similar to that of SN 2016gkg. We note that the temporal cadence of the follow-up observations of these SNe are good enough to map the periodic bumps in their light curves (see Figure 8).

In the case of SN 2016gkg, we see flux density enhancement at $t \sim 299$ days, which correspond to a stellar evolution phase of ~48 yr prior to explosion for $v_{\rm w} \sim 200\,{\rm km\,s^{-1}}$. Kilpatrick et al. (2017) suggested a binary progenitor model for SN 2016gkg where the initial period of the binary orbit is ~1000 days (2.7 yr). This periodicity will be seen as another flux density enhancement at $t \sim 313$ days for the derived shock velocities. This epoch is not sampled in the observations. Thus even if there is a binary companion and related periodicity in the density distribution of the CSM, the radio data do not have a temporal cadence to probe those fluctuations, and we cannot rule out the binary scenario.

The radio luminosity is related to the density of the CSM as $L \propto \rho_{\rm CSM}^{(p-7+12m)/4}$, where $\rho_{\rm CSM} \propto (\dot{M}/v_{\rm w})$ (Ryder et al. 2004). In the case of SN 2016gkg, the best-fit value of $p = 3$ and $m = 0.8$ indicates that a factor of 2 increase in radio flux density indicates ~70% increase in the CSM density. The effect of density enhancement is reflected in the evolution of shock radii and magnetic field as well (see Figure 6). The magnetic field is slightly enhanced compared to its expected regular temporal evolution and there is a slight change in the expansion of the shock wave at the same time. The magnetic field is enhanced by a factor of 1.6 in comparison to the extrapolation of its evolution in the previous phases. The additional thermal energy produced due to these density enhancements increases the B. A similar increase in the B value by a factor of 1.3 is seen in SN 2003bg during its first

Table 4
Blast-wave Parameters of SN 2016gkg

Age[a] (Day)	F_p (mJy)	ν_p (GHz)	α ...	χ^2_μ ...	R ($\times 10^{15}$cm)	B (Gauss)	V_s ($\times 10^4$km s^{-1})	$\dot{M}$ ($\times 10^{-6}$ $M_\odot$ yr^{-1})
24	$1.55^{0.18}_{-0.16}$	$8.96^{0.68}_{-0.65}$	$-0.80^{0.20}_{-0.22}$	1.72	$5.09^{0.68}_{-0.66}$	$1.03^{0.08}_{-0.08}$	$2.46^{0.33}_{-0.32}$	$2.20^{0.90}_{-0.86}$
49	$2.20^{0.14}_{-0.14}$	$5.82^{0.26}_{-0.25}$	$-1.49^{0.13}_{-0.13}$	3.30	$9.26^{1.01}_{-1.00}$	$0.65^{0.03}_{-0.03}$	$2.19^{0.24}_{-0.24}$	$3.58^{1.16}_{-1.16}$
86	$2.22^{0.14}_{-0.14}$	$3.43^{0.28}_{-0.23}$	$-1.25^{0.09}_{-0.09}$	0.66	$15.77^{2.02}_{-1.90}$	$0.38^{0.03}_{-0.03}$	$2.13^{0.27}_{-0.26}$	$3.82^{1.52}_{-1.40}$
299	$2.28^{0.19}_{-0.19}$	$1.79^{0.12}_{-0.13}$	$-1.19^{0.09}_{-0.09}$	0.98	$30.59^{3.70}_{-3.81}$	$0.20^{0.01}_{-0.01}$	$1.18^{0.14}_{-0.15}$	$12.56^{4.62}_{-4.80}$
330	$1.62^{0.15}_{-0.14}$	$0.85^{0.06}_{-0.06}$	$-0.92^{0.07}_{-0.07}$	0.72	$55.08^{6.88}_{-6.93}$	$0.10^{0.01}_{-0.01}$	$1.93^{0.24}_{-0.24}$	$3.68^{1.42}_{-1.42}$
492	$1.79^{0.15}_{-0.14}$	$0.67^{0.06}_{-0.06}$	$-1.07^{0.05}_{-0.05}$	1.63	$72.57^{9.51}_{-10.00}$	$0.08^{0.01}_{-0.01}$	$1.71^{0.22}_{-0.24}$	$5.02^{2.06}_{-2.20}$

Note.
[a] The age is calculated using 2016 September 20.15 (UT) as the date of explosion (Kilpatrick et al. 2017).
F_p, ν_p, and α denote the peak flux density, peak frequency, and optically thin spectral index in the best-fit SSA model at each epoch. R, B, V, and $\dot{M}$ denote shock radius, magnetic field, mass-loss rate, and mean shock velocity, respectively.

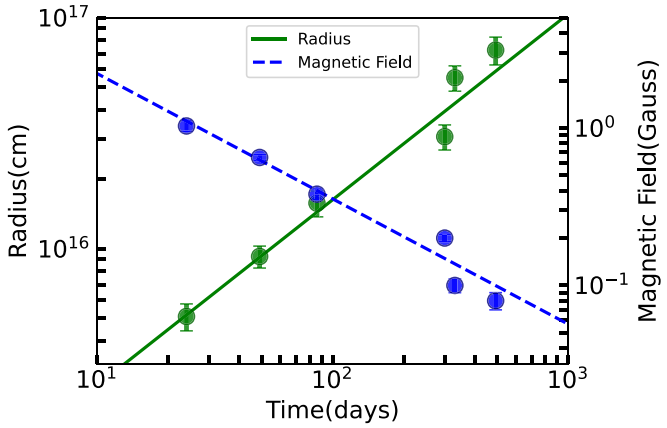

Figure 6. The shock radii (green filled circles) and magnetic fields (blue filled circles) at $t \sim 24$, 49, 86, 299, 330, and 492 days postexplosion. The green solid line denotes a power-law fit to the shock radii; $R \sim t^{0.80\pm0.08}$ and blue solid line denotes a power-law fit to the magnetic field: $B \sim t^{-0.80\pm0.09}$.

light-curve bump (Soderberg et al. 2006). To summarize, there is a close resemblance between SN 2016gkg, SN 2003bg, and SN 2001ig in terms of the timescale and strength of flux density enhancement in late-time radio light curves.

6. Discussion

The shock velocities of SN 2016gkg derived from SSA modeling is $v \sim 24{,}600$ km s^{-1} ($v \sim 0.1c$) at $t \sim 24$ days. The velocities estimated from optical lines at $t \sim 21$ days are $v \sim 12{,}200$ km s^{-1} (Tartaglia et al. 2017). Thus the shock wave is traveling with a velocity a factor of 2 faster than the material in the photosphere. The SSA-derived shock velocity is greater than the velocities from optical lines and indicates that FFA is not contributing much in defining the peak of the light curve/spectra. We also note that the FFA models were resulting in higher χ^2_μ values while modeling. The radio data being inconsistent with the FFA model and the relatively higher shock velocity of $v \sim 0.1c$ are indicative of a compact progenitor star with faster stellar winds.

The temporal evolution of shock wave radius is best fitted by a power law $R \propto t^{0.80\pm0.08}$. The m value will be 1, for a nondecelerating blast wave and the derived m value indicates a decelerating blast wave. The temporal index of the postshock magnetic field is found to be $\alpha_B = -0.8 \pm 0.1$ ($B \propto t^{\alpha_B}$); α_B can be connected to the CSM density as $\alpha_B = [m(2-s)/2] - 1$, which gives $s = 1.5$. Thus the CSM density is slightly flatter than the one created by a steady stellar wind. The derived values of m and s indicate an ejecta density profile of $\rho_{\rm ejecta} \propto r^{-9}$ ($m = n - 3/n - s$), consistent with a low-mass compact progenitor (Chevalier 1998). Assuming $\epsilon_B = 0.33$ and $v_w = 200$ km s^{-1}, the mass-loss rate of the progenitor is in the range $\dot{M} \sim (2.2\text{–}5.0) \times 10^{-6}$ $M_\odot$ yr^{-1}, at $t \sim 24$, 49, 86, 330, and 492 days. The mass-loss rate corresponding to $t \sim 299$ days is $\dot{M} \sim 12.6 \times 10^{-6}$ $M_\odot$ yr^{-1}, a factor of three higher than the $\dot{M}$ values at other epochs. This is suggestive of an enhanced phase of mass loss at ~48 yr prior to explosion for the assumed wind speed as discussed in Section 5.

6.1. Comparison with Other Radio Bright SNe IIb

We view the radio properties of SN 2016gkg in comparison with other radio bright SNe IIb events in Figure 7. We compile all SNe IIb with well-sampled light curves/spectra that define F_p, ν_p, and t_p in the L_p–t_p diagram (also see Table 5). The dotted lines indicate the mean shock velocities in an SSA scenario for $p = 3$ assuming the equipartition of energy between relativistic particles and magnetic fields ($\epsilon_B = \epsilon_e$). This plot is an updated version of a similar plot presented in Chevalier & Soderberg (2010). The authors compiled radio properties of a sample of SNe IIb and divided them into two populations based on their position in the L_p–t_p diagram: one is SNe IIb with compact progenitors (SNe cIIb) and the other with extended progenitors (SNe eIIb). The SNe cIIb group consists of SN 2008ax, SN 2003bg, and SN 2001ig, which has faster shocks, a less dense CSM, and a compact progenitor in comparison with the SNe eIIb (like SN 1993J and SN 2001gd). SNe eIIb have slower shocks owing to their denser CSM from slow stellar winds of extended progenitors.

SNe IIb show peak spectral luminosities that span 2 orders of magnitude, and the peak time varies over a factor of ~40. This broad distribution in peak spectral luminosities and rise times indicates the variety in the intrinsic properties of their progenitors. There are only five SNe IIb (including SN 2016gkg) that have progenitors identified from preexplosion images. It is important to tie up the radio properties of these SNe with the inferences from preexplosion imaging analysis. The progenitor of SN 1993J is identified to be a yellow supergiant star of radius ~600 $R_\odot$ (Aldering et al. 1994) from preexplosion images. Similarly, an extended progenitor of radius $\sim 545 \pm 65$ $R_\odot$ was identified as the progenitor of SN 2013df (Van Dyk et al. 2014). A slightly less extended star of radius ~200 $R_\odot$ was identified as the progenitor of

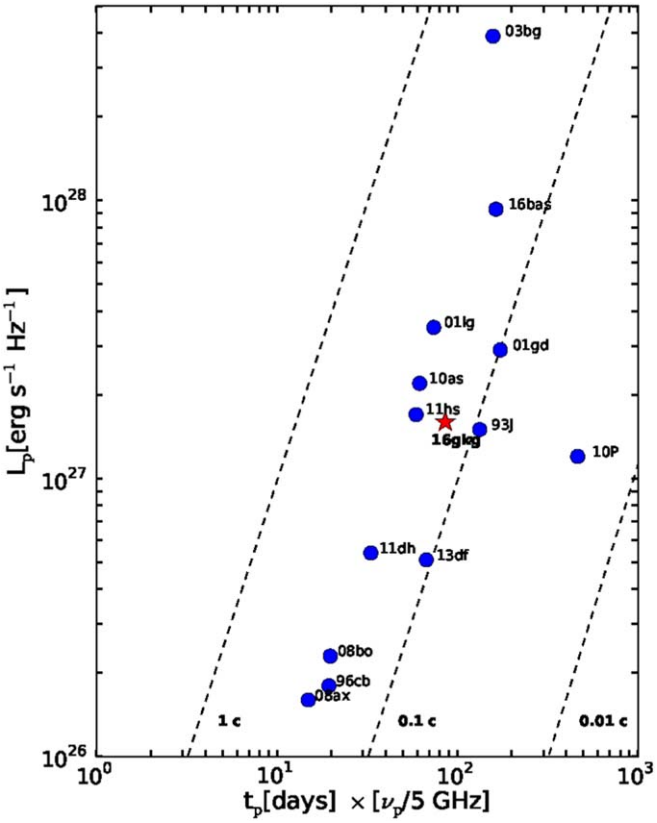

Figure 7. The peak radio spectral luminosities vs. time of peak of the light curves are plotted for all well-observed SNe IIb in the literature. Each SNe is denoted by the last two digits of the year of explosion and last two letters of the name. The dotted lines represent the mean velocity of the radio emitting shell if SSA is the dominant absorption process that defines the peak of the light curve (Chevalier 1998) and for $p = 3$.

SN 2011dh (Van Dyk et al. 2013). However, the presence of a binary companion has been speculated for this SN (Van Dyk et al. 2013), and Arcavi et al. (2011) suggested the progenitor of SN 2011dh to be a relatively compact star from the analysis of a series of spectra and bolometric light curves. The authors also argued that the larger radius ($R \sim 10^{13}$ cm) derived from preexplosion HST images could be due to the identification of a blended source. The progenitor of SN 2008ax was identified to be of radius $\sim$30−50 $R_\odot$ (Folatelli et al. 2015). These estimates of progenitor radius from pre-SN image analysis are roughly consistent with the radio-derived properties—SN 1993J and SN 2013df to have more extended progenitors whereas SN 2008ax and SN 2011dh to have relatively compact progenitors with a higher shock velocity (see Figure 7). In light of these results, one can also argue that the classification of SNe IIb progenitors into two categories as eSNe IIb and cSNe IIb (Chevalier & Soderberg 2010) is rather simplistic and the progenitor properties could be a continuum between these two. The position of SN 2016gkg in this diagram is among SNe cIIb, toward the right of SN 2008ax. This could imply that the progenitor of SN 2016gkg is a relatively compact progenitor with a radius slightly more than that of SN 2008ax, i.e., 50 $R_\odot$.

6.2. Inferences on the Progenitor

Multiple pieces of evidence from radio modeling are in favor of a compact progenitor for SN 2016gkg. The broad agreement

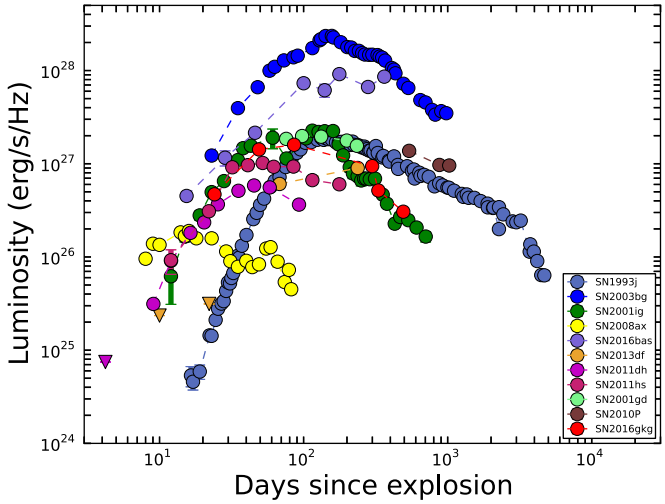

Figure 8. 5 GHz radio light curves of well-observed SNe IIb. Flux measurements are taken from Weiler et al. (2007) for SN 1993J, Soderberg et al. (2006) for SN 2003bg, Ryder et al. (2004) for SN 2001ig, Roming et al. (2009) for SN 2008ax, Bietenholz et al. (2021) for SN 2016bas, Kamble et al. (2016) for SN 2013df, Krauss et al. (2012) for SN 2011dh, Bufano et al. (2014) for SN 2011hs, Stockdale et al. (2007) for SN 2001gd, Romero-Cañizales et al. (2014) for SN 2010P, and this work for SN 2016gkg.

of multifrequency radio data with an SSA model indicates that the CSM is relatively rarer created due to faster stellar winds from a compact star. The mean shock velocities ($v \sim 0.1c$) derived from SSA formulation are difficult to incorporate in the framework of a shock breakout from an extended progenitor (Nakar & Sari 2010).

A correlation between $\dot{M}$ values and progenitor radius of SNe IIb is proposed by Maeda et al. (2015) and Kamble et al. (2016), where the extended progenitors experience stronger mass loss toward their end of life compared to compact progenitors. The progenitor mass-loss rate of SN 2016gkg derived from the shock parameters at $t \sim 24$ days is $\dot{M} \sim 2.2 \times 10^{-6}\ M_\odot\ \mathrm{yr}^{-1}$, comparable to the $\dot{M}$ values derived for SN 2008ax (Roming et al. 2009). These $\dot{M}$ values are an order of magnitude lower than that of SN 1993J and SN 2013df (see Table 5), which are known to have extended progenitors from direct detection efforts. Thus the $\dot{M}$ estimates also imply a relatively compact progenitor.

The best-fit value of the electron power-law index is $p \sim 3$, typically found for SNe Ibc that are presumed to have compact Wolf–Rayet stars as progenitors. Late-time variability in the radio light curves is an important observational characteristic of SNe cIIb progenitors (e.g., SN 2001ig, SN 2003bg; Ryder et al. 2004; Soderberg et al. 2006). All SNe cIIb except SN 2011dh with well-sampled radio light curves exhibit fluctuations indicative of density modulations in the CSM (see Figure 8). These density fluctuations could be due to the variability in the stellar winds of compact stars or due to the influence of a binary companion. The radio observations of SN 2011dh probe a radius up to 1.5×10^{16} cm that translates to a $\sim$5 yr prior explosion for a $v_w \sim 1000\ \mathrm{km\ s}^{-1}$, which could be shorter for any substantial wind variability (Krauss et al. 2012). We see similar late-time flux density enhancement in the radio light curves of SN 2016gkg. The position of SN 2016gkg in the $L_p - t_p$ diagram is in the contour of SNe cIIb, indicating a progenitor radius slightly more than that of SN 2008ax (i.e., >50 $R_\odot$).

Table 5
Properties of Well-studied Type IIb Supernovae

SN	Distance (Mpc)	ν_p (GHz)	t_p (days)	F_p (mJy)	L_p (erg s^{-1} Hz^{-1})	$\dot{M}$ ($M_\odot$ yr^{-1})	References
SN 1993J	3.6	5	133	96.9	1.5×10^{27}	$(2-6) \times 10^{-5}$	1
SN 1996cb	9.1	5	19.4	1.8	1.8×10^{26}	⋯	2
SN 2001gd	17.5	5	173	8.0	2.9×10^{27}	3×10^{-5}	3
SN 2001ig	11.5	5	74	22	3.5×10^{27}	8.6×10^{-5}	4
SN 2003bg	19.6	22.5	35	85	3.9×10^{28}	6.1×10^{-5}	5
SN 2008ax	6.2	4.86	15.34	3.54	1.6×10^{26}	$(1\text{-}6) \times 10^{-6}$	6
SN 2008bo	19.1	8.5	11.6	0.52	2.3×10^{26}	⋯	7
SN 2010P	44.8	5	464	0.52	1.2×10^{27}	$(3.0-5.1) \times 10^{-5}$	8
SN 2010as	27.4	9	34.3	2.43	2.2×10^{27}	⋯	7
SN 2011dh	7.9	4.7	35.3	7.3	5.4×10^{26}	6×10^{-5}	9
SN 2011hs	26.4	5	59	2.0	1.7×10^{27}	2×10^{-5}	10
SN 2013df	16.6	5	67.3	1.55	5.1×10^{26}	8×10^{-5}	11
SN 2016bas	42.4	5.5	148.8	4.33	9.3×10^{27}	⋯	7
SN 2016gkg	26.4	5	85.86	1.92	1.6×10^{27}	3.8×10^{-6}	12

Note. The listed $\dot{M}$ values are taken from the literature as cited in the last column of the table. These values are strongly dependent on the assumed wind velocities.
References. (1) Fransson et al. (1996), (2) Weiler et al. (1998), (3) Stockdale et al. (2003), (4) Ryder et al. (2004), (5) Soderberg et al. (2006), (6) Roming et al. (2009), (7) Bietenholz et al. (2021), (8) Romero-Cañizales et al. (2014), (9) Soderberg et al. (2012), (10) Bufano et al. (2014), (11) Kamble et al. (2016), (12) this work.
Among the listed SNe, five of them have progenitor detections from archival images. They are SN 1993J (Aldering et al. 1994), SN 2013df (Van Dyk et al. 2014), SN 2008ax (Folatelli et al. 2015), SN 2011dh (Arcavi et al. 2011; Van Dyk et al. 2013), and SN 2016gkg (Kilpatrick et al. 2017, 2021; Tartaglia et al. 2017).

Table 6
Compilation of the Radius Estimates of the Progenitor of SN 2016gkg from the Literature

Radius ($R_\odot$)	Method	Reference
138^{+131}_{-103}	Archival HST imaging analysis[a]	Kilpatrick et al. (2017)
150–320	Archival HST imaging analysis[a]	Tartaglia et al. (2017)
∼70	Archival HST imaging analysis[b]	Kilpatrick et al. (2021)
257^{+389}_{-189}	Analytical shock cooling model[c]	Kilpatrick et al. (2017)
48–124	Analytical shock cooling model[c]	Tartaglia et al. (2017)
40–150	Analytical shock cooling model[d]	Arcavi et al. (2017)
180–260	Numerical shock cooling model	Piro et al. (2017)
∼320 $R_\odot$	Numerical shock cooling model	Bersten et al. (2018)

Notes.
[a] Kilpatrick et al. (2017) and Tartaglia et al. (2017) used Keck and Very Large Telescope + Nasmyth adaptive optics systems, respectively, to perform relative astrometry. Kilpatrick et al. (2017) considered one progenitor candidate and Tartaglia et al. (2017) considered two progenitor candidates.
[b] Postexplosion HST imaging of the field containing SN 2016gkg was used to perform relative astrometry.
[c] Kilpatrick et al. (2017) and Tartaglia et al. (2017) modeled the luminosity (up to $t \sim 1.5$ days) and temperature evolution (up to $t \sim 5$ days), respectively, using the Rabinak & Waxman (2011) model.
[d] Analytic shock cooling models (Nakar & Piro 2014; Piro 2015; Sapir & Waxman 2017).

The radius estimates of the progenitor from shock cooling models span a wide range ∼40–646 $R_\odot$ (see Table 6; Arcavi et al. 2017; Kilpatrick et al. 2017; Piro et al. 2017; Tartaglia et al. 2017; Bersten et al. 2018). One can argue that the radio-derived constraints of a compact progenitor are broadly in agreement with the results from shock cooling models. The large range of radius estimates from these models will be in agreement with an extended progenitor model as well.

Kilpatrick et al. (2017) and Tartaglia et al. (2017) determined the progenitor radii to be $R = 138^{+131}_{-103}$ $R_\odot$ and $R = 150-320$ $R_\odot$, respectively, from the preexplosion HST imaging analysis of the field containing SN 2016gkg. Relative astrometry was done using the Keck and Very Large Telescope adaptive optics system in these studies. The late-time HST imaging of the field of SN 2016gkg using the advanced camera for surveys (ACS) and the wide field camera 3 (WFC 3) resulted in superior resolution and improved astrometric alignment between the SN and progenitor candidate (Kilpatrick et al. 2021). The updated photometric analysis suggests the progenitor to be a yellow supergiant of mass 10^{+2}_{-1} $M_\odot$ and radius ∼70 $R_\odot$. Thus the inferences on the progenitor star from radio analyses are in agreement with that derived from preexplosion imaging analysis (Kilpatrick et al. 2021).

7. Conclusions

We present long-term ($t \sim 8$–1429) radio monitoring of SN 2016gkg over a frequency range $\nu \sim 0.3$–24 GHz to investigate the properties of its progenitor and the CSM. The inferences from our observations and modeling can be summarized as follows.

1. The radio data is best represented by a self-absorbed synchrotron emission that arises due to the interaction of an SN shock wave of $v \sim 0.1c$ propagating into a CSM created due to the mass loss of the progenitor star.
2. The CSM density is found to have moderate density fluctuation at a distance $R \sim 3.1 \times 10^{16}$ cm, likely due to enhancement in the progenitor mass-loss rate or due to the effect of a binary companion. Assuming a stellar wind velocity $v_w \sim 200$ km s^{-1}, this corresponds to a stellar evolution phase ∼48 yr prior to explosion.
3. We estimate the average mass-loss rate to be $\dot{M} \sim 3.7 \times 10^{-6}$ $M_\odot$ yr^{-1} during 8 to 115 yr before explosion, with a factor of ∼3 higher $\dot{M}$ at ∼48 yr prior to explosion.
4. The radio data being consistent with the SSA model, shock velocities of $v \sim 0.1c$, the position of SN 2016gkg in the region of SNe cIIb in the L_p–t_p diagram, and late-time modest variability in radio flux densities are suggestive of a compact progenitor star.

We thank the staff of the GMRT that made these observations possible. GMRT is run by the National Centre for Radio Astrophysics of the Tata Institute of Fundamental Research. The National Radio Astronomy Observatory is a facility of the National Science Foundation operated under cooperative agreement by Associated Universities, Inc. Nayana A.J. acknowledges DST- INSPIRE Faculty Fellowship (IFA20-PH-259) for supporting this research. P.C. acknowledges the support of the Department of Atomic Energy, Government of India, under project No. 12-R&D-TFR-5.02-0700.

Facilities: GMRT, VLA.

Software: CASA (McMullin et al. 2007), AIPS (van Moorsel et al. 1996), emcee (Foreman-Mackey et al. 2013).

ORCID iDs

Nayana A. J. https://orcid.org/0000-0002-8070-5400
Poonam Chandra https://orcid.org/0000-0002-0844-6563
G. C. Anupama https://orcid.org/0000-0003-3533-7183

References

Aldering, G., Humphreys, R. M., & Richmond, M. 1994, AJ, 107, 662
Arcavi, I., Gal-Yam, A., Yaron, O., et al. 2011, ApJL, 742, L18
Arcavi, I., Hosseinzadeh, G., Brown, P. J., et al. 2017, ApJL, 837, L2
Baron, E., Hauschildt, P. H., Branch, D., et al. 1993, ApJL, 416, L21
Bersten, M. C., Benvenuto, O. G., Nomoto, K., et al. 2012, ApJ, 757, 31
Bersten, M. C., Folatelli, G., García, F., et al. 2018, Natur, 554, 497
Bietenholz, M. F., Bartel, N., Argo, M., et al. 2021, ApJ, 908, 75
Björnsson, C.-I., & Keshavarzi, S. T. 2017, ApJ, 841, 12
Bufano, F., Pignata, G., Bersten, M., et al. 2014, MNRAS, 439, 1807
Chandra, P., Nayana, A. J., Björnsson, C.-I., et al. 2019, ApJ, 877, 79
Chevalier, R. A. 1982, ApJ, 259, 302
Chevalier, R. A. 1996, ASP Conf. Ser. 93: Radio Emission from the Stars and the Sun, 93 (Cambridge: Cambridge Univ. Press), 125
Chevalier, R. A. 1998, ApJ, 499, 810
Chevalier, R. A., & Soderberg, A. M. 2010, ApJL, 711, L40
Condon, J. J., Cotton, W. D., Greisen, E. W., et al. 1998, AJ, 115, 1693
Crockett, R. M., Eldridge, J. J., Smartt, S. J., et al. 2008, MNRAS, 391, L5
Drout, M. R., Massey, P., Meynet, G., et al. 2009, ApJ, 703, 441
Filippenko, A. V. 1997, ARA&A, 35, 309
Folatelli, G., Bersten, M. C., Kuncarayakti, H., et al. 2015, ApJ, 811, 147
Foreman-Mackey, D., Conley, A., Meierjurgen Farr, W., et al. 2013, PASP, 125, 306
Fransson, C., Lundqvist, P., & Chevalier, R. A. 1996, ApJ, 461, 993
Fuller, J., & Ro, S. 2018, MNRAS, 476, 1853
Greisen, E. W. 2003, in Information Handling in Astronomy—Historical Vistas, ed. A. Heck, 285 (Dordrecht: Kluwer Academic), 109
Ho, A. Y. Q., Phinney, E. S., Ravi, V., et al. 2019, ApJ, 871, 73
Horesh, A., Stockdale, C., Fox, D. B., et al. 2013, MNRAS, 436, 1258
Kamble, A., Margutti, R., Soderberg, A. M., et al. 2016, ApJ, 818, 111
Kilpatrick, C. D., Coulter, D. A., Foley, R. J., et al. 2021, arXiv:2112.03308
Kilpatrick, C. D., Foley, R. J., Abramson, L. E., et al. 2017, MNRAS, 465, 4650
Krauss, M. I., Soderberg, A. M., Chomiuk, L., et al. 2012, ApJL, 750, L40
Kuncarayakti, H., Folatelli, G., Maeda, K., et al. 2020, ApJ, 902, 139
Maeda, K., Hattori, T., Milisavljevic, D., et al. 2015, ApJ, 807, 35
Maeda, K., Katsuda, S., Bamba, A., et al. 2014, ApJ, 785, 95
Maund, J. R., Fraser, M., Ergon, M., et al. 2011, ApJL, 739, L37
Maund, J. R., Smartt, S. J., Kudritzki, R. P., et al. 2004, Natur, 427, 129
McMullin, J. P., Waters, B., Schiebel, D., et al. 2007, in Astronomical Data Analysis Software and Systems XVI, ASP Conf. Ser. 376 (Cambridge: Cambridge Univ. Press), 127
Montes, M. J., Weiler, K. W., Van Dyk, S. D., et al. 2000, ApJ, 532, 1124
Nakar, E., & Piro, A. L. 2014, ApJ, 788, 193
Nakar, E., & Sari, R. 2010, ApJ, 725, 904
Nasonova, O. G., de Freitas Pacheco, J. A., & Karachentsev, I. D. 2011, A&A, 532, A104
Nayana, A. J., & Chandra, P. 2020, MNRAS, 494, 84
Nayana, A. J., & Chandra, P. 2021, ApJL, 912, L9
Nayana, A. J., Chandra, P., & Ray, A. K. 2018, ApJ, 863, 163
Nayana, A. J., Chandra, P., Roy, S., et al. 2017, MNRAS, 467, 155
Piro, A. L. 2015, ApJL, 808, L51
Piro, A. L., Muhleisen, M., Arcavi, I., et al. 2017, ApJ, 846, 94
Podsiadlowski, P., Joss, P. C., & Hsu, J. J. L. 1992, ApJ, 391, 246
Rabinak, I., & Waxman, E. 2011, ApJ, 728, 63
Romero-Cañizales, C., Herrero-Illana, R., Pérez-Torres, M. A., et al. 2014, MNRAS, 440, 1067
Roming, P. W. A., Pritchard, T. A., Brown, P. J., et al. 2009, ApJL, 704, L118
Ryder, S. D., Sadler, E. M., Subrahmanyan, R., et al. 2004, MNRAS, 349, 1093
Sahu, D. K., Anupama, G. C., & Chakradhari, N. K. 2013, MNRAS, 433, 2
Sapir, N., & Waxman, E. 2017, ApJ, 838, 130
Smith, N. 2014, ARA&A, 52, 487
Smith, N., & Conti, P. S. 2008, ApJ, 679, 1467
Soderberg, A. M., Chevalier, R. A., Kulkarni, S. R., et al. 2006, ApJ, 651, 1005
Soderberg, A. M., Margutti, R., Zauderer, B. A., et al. 2012, ApJ, 752, 78
Stockdale, C. J., Weiler, K. W., Van Dyk, S. D., et al. 2003, ApJ, 592, 900
Stockdale, C. J., Williams, C. L., Weiler, K. W., et al. 2007, ApJ, 671, 689
Swartz, D. A., Clocchiatti, A., Benjamin, R., et al. 1993, Natur, 365, 232
Tartaglia, L., Fraser, M., Sand, D. J., et al. 2017, ApJL, 836, L12
Taubenberger, S., Navasardyan, H., Maurer, J. I., et al. 2011, MNRAS, 413, 2140
Van Dyk, S. D., Zheng, W., Clubb, K. I., et al. 2013, ApJL, 772, L32
Van Dyk, S. D., Zheng, W., Fox, O. D., et al. 2014, AJ, 147, 37
van Moorsel, G., Kemball, A., & Greisen, E. 1996, in Astronomical Data Analysis Software and Systems V, ASP Conf. Ser. 101, ed. G. H. Jacoby & J. Barnes (Cambridge: Cambridge Univ. Press), 37
Weiler, K. W., Panagia, N., Montes, M. J., et al. 2002, ARA&A, 40, 387
Weiler, K. W., Sramek, R. A., Panagia, N., et al. 1986, ApJ, 301, 790
Weiler, K. W., Van Dyk, S. D., Montes, M. J., et al. 1998, ApJ, 500, 51
Weiler, K. W., van Dyk, S. D., Pringle, J. E., et al. 1992, ApJ, 399, 672
Weiler, K. W., Williams, C. L., Panagia, N., et al. 2007, ApJ, 671, 1959
Yoon, S.-C., Dessart, L., & Clocchiatti, A. 2017, ApJ, 840, 10
Yoon, S.-C., Woosley, S. E., & Langer, N. 2010, ApJ, 725, 940